Identification of tidal features in deep optical galaxy images with convolutional neural networks

H. Domínguez Sánchez [1,2]★ G. Martin [3,4] I. Damjanov,[5] F. Buitrago [6,7] M. Huertas-Company [8,9,10]
C. Bottrell,[11] M. Bernardi,[12] J. H. Knapen,[8,9] J. Vega-Ferrero [6,8,9] R. Hausen,[13] E. Kado-Fong [14]
D. Población-Criado,[15] H. Souchereau,[5,16] O. K. Leste,[17] B. Robertson,[18] B. Sahelices[15] and K.
V. Johnston[19]

[1]*Centro de Estudios de Física del Cosmos de Aragón (CEFCA), Plaza San Juan, 1, E-44001 Teruel, Spain*
[2]*Institute of Space Sciences (ICE, CSIC), Campus UAB, Carrer de Can Magrans, s/n, E-08193 Barcelona, Spain*
[3]*Korea Astronomy and Space Science Institute, 776 Daedeokdae-ro, Yuseong-gu, Daejeon 34055, Korea*
[4]*Steward Observatory, University of Arizona, 933 N. Cherry Ave, Tucson, AZ 85719, USA*
[5]*Department of Astronomy and Physics, Saint Mary's University, 923 Robie Street, Halifax, NS B3H 3C3, Canada*
[6]*Departamento de Física Teórica, Atómica y Óptica, Universidad de Valladolid, E-47011 Valladolid, Spain*
[7]*Instituto de Astrofísica e Ciências do Espaço, Universidade de Lisboa, OAL, Tapada da Ajuda, PT1349-018 Lisbon, Portugal*
[8]*Instituto de Astrofísica de Canarias (IAC), La Laguna E-38205, Spain*
[9]*Departamento de Astrofísica - Universidad de La Laguna, La Laguna E-38205, Spain*
[10]*LERMA - Observatoire de Paris, PSL, Université Paris-Cité, Paris, F-75014, France*
[11]*Kavli Institute for the Physics and Mathematics of the Universe (WPI), UTIAS, University of Tokyo, Kashiwa, Chiba 277-8583, Japan*
[12]*Department of Physics and Astronomy, University of Pennsylvania, Philadelphia, PA 19104, USA*
[13]*Department of Physics and Astronomy, The Johns Hopkins University, 3400 N. Charles St., Baltimore, MD 21218 USA*
[14]*Physics Department, Yale Center for Astronomy & Astrophysics, PO Box 208120, New Haven, CT 06520, USA*
[15]*GCME Research Group, Departamento de Informática, Universidad de Valladolid, E-47011 Valladolid, Spain*
[16]*Department of Astronomy, Yale University, New Haven, CT 06511, USA*
[17]*Department of Physics and Astronomy, University of Victoria, 3800 Finnerty Rd, Victoria, BC V8P 5C2, Canada*
[18]*Department of Astronomy and Astrophysics, University of California, Santa Cruz, 1156 High Street, Santa Cruz, CA 95064 USA*
[19]*Department of Astronomy, Columbia University, New York, NY, USA*

ABSTRACT

Interactions between galaxies leave distinguishable imprints in the form of tidal features, which hold important clues about their mass assembly. Unfortunately, these structures are difficult to detect because they are low surface brightness features, so deep observations are needed. Upcoming surveys promise several orders of magnitude increase in depth and sky coverage, for which automated methods for tidal feature detection will become mandatory. We test the ability of a convolutional neural network to reproduce human visual classifications for tidal detections. We use as training ∼6000 simulated images classified by professional astronomers. The mock Hyper Suprime Cam Subaru (HSC) images include variations with redshift, projection angle, and surface brightness ($\mu_{\mathrm{lim}} = 26$–35 mag arcsec^{-2}). We obtain satisfactory results with accuracy, precision, and recall values of Acc = 0.84, $P = 0.72$, and $R = 0.85$ for the test sample. While the accuracy and precision values are roughly constant for all surface brightness, the recall (completeness) is significantly affected by image depth. The recovery rate shows strong dependence on the type of tidal features: we recover all the images showing *shell* features and 87 per cent of the tidal *streams*; these fractions are below 75 per cent for *mergers, tidal tails*, and *bridges*. When applied to real HSC images, the performance of the model worsens significantly. We speculate that this is due to the lack of realism of the simulations, and take it as a warning on applying deep learning models to different data domains without prior testing on the actual data.

Key words: methods: observational – software: development – galaxies: interactions – galaxies: structure.

1 INTRODUCTION

In the standard Λ-Cold Dark Matter (ΛCDM) cosmology scenario, small-scale overdense perturbations in the early Universe collapse first, and produce dark matter haloes that accumulate baryons at the centre. The small structures aggregate successively into larger structures via mergers in a process known as hierarchical growth (White & Rees [1978]; Fall & Efstathiou [1980]; White & Frenk [1991]; Lacey & Cole [1993]). In addition, accretion processes of small satellite galaxies or gas in filaments produce a vast and complex network of ultra-low surface brightness streams, which should be

★ E-mail: hdominguez@cefca.es

present around all galaxies (e.g. Pillepich et al. 2014 and references therein).

Therefore, galaxy mergers have a fundamental and critical role within the ΛCDM cosmogony. While there is a general consensus that the merger fraction increases with galaxy stellar mass, both from simulations (e.g. Rodriguez-Gomez et al. 2016; Huško, Lacey & Baugh 2022) and observations (van Dokkum et al. 2010; López-Sanjuan et al. 2012; Rodríguez-Puebla et al. 2017), the relative contribution of *in situ* star formation and accreted stellar mass remains an open question across much of the galaxy mass spectrum (e.g. Qu et al. 2017; Fitts et al. 2018; Conselice et al. 2022). The rate of major and minor merger events, and their impact on galaxy mass assembly and morphological transformations, are also under debate (e.g. Lotz et al. 2011; Lofthouse et al. 2017; Martin et al. 2017, 2018, 2021).

Minor mergers (with baryonic mass ratios below 1:4) are expected to be significantly more common than major ones (e.g. Cole et al. 2000; Lotz et al. 2011), and to remain frequent even at the present epoch (although this is still under debate, see for example O'Leary et al. 2021). As minor mergers do not necessarily destroy pre-existing stellar discs (e.g. Robertson et al. 2006), signs of recent or ongoing minor mergers should be apparent around galaxies in the form of stellar tidal features, which extend into the halo of the central galaxy. Merger remnants, which are only a few dynamical periods old, should leave distinguishable imprints in the outskirts of galaxies. The frequency and characteristics of these features hold vital clues to the nature of the events which have created them (Hernquist & Quinn 1989; Mihos, Dubinski & Hernquist 1998; Helmi & White 1999; Martínez-Delgado et al. 2009; Hendel & Johnston 2015; Montes et al. 2020; Spavone et al. 2020; Vera-Casanova et al. 2022), and can thus be used to disentangle the different formation channels. Following Duc et al. (2015), *tails* are expected to be pulled out material from a gas-rich disc galaxy, while *streams* would be stripped material from a low-mass companion being consumed by the primary galaxy. Other features such as *fans* and *plumes* are expected to come from dry, major mergers. In addition, *clouds* and *shells* are expected to be the result of interactions with radial orbits, while *great circles* are more predominant for circular orbits events (Johnston et al. 2008).

Unfortunately, the majority of tidal features have very low surface brightness, expected to be fainter than 29 mag arcsec^{-2} in the *r*-band (Bullock & Johnston 2005; Cooper et al. 2013), and extremely deep observations are necessary to detect them, as shown explicitly in Conselice, Bershady & Jangren (2000), Ji, Peirani & Yi (2014), Bottrell et al. (2019a), Thorp et al. (2021) and Mancillas et al. (2019), where the authors find two and three times more streams based on a surface brightness cut-off 33 mag arcsec^{-2} than with 29 mag arcsec^{-2}. Although there is an increasing interest in the literature on the identification and characterization of tidal features, most works focus on the detailed analysis of a small number of objects via visual inspection (e.g. Martínez-Delgado et al. 2010; Javanmardi et al. 2016; Morales et al. 2018; Martinez-Delgado et al. 2021; Huang & Fan 2022; Sola et al. 2022; Valenzuela & Remus 2022), some of them belong to local groups or clusters of galaxies (e.g. Iodice et al. 2017; Mihos et al. 2017; Spavone et al. 2018). A sample of 92 ETGs galaxies from ATLAS^{3D} was presented in Duc et al. (2015), reporting signs of interactions or perturbed morphologies in more than half of them, thanks to an observing strategy and data reduction pipeline optimized for low surface brightness features. Hood et al. (2018) present a visual identification of galaxies with tidal features based on DECam Legacy Survey images (*r*-band 3σ depth of ~27.9 mag arcsec^{-2}),

but due to the small area inspected (100 arcsec^2), less than 200 of them have tidal features detected with high confidence. One of the largest catalogues of tidal detections up to date was presented in Kado-Fong et al. (2018) using The Hyper Suprime-Cam Subaru Strategic Program (HSC-SSP, Miyazaki et al. 2012) data. The authors applied applied a filtering algorithm that iteratively separates low- and high-spatial frequency features of images, resulting in a sample of ~1200 galaxies with tidal detections from a sample of ~20 000.

With the arrival of large imaging surveys such as Euclid (Laureijs et al. 2011) and the Vera Rubin Observatory's Legacy Survey of Space and Time (LSST; Ivezić et al. 2019), the detection of these features via visual inspection is unfeasible and automated methods become imperative. The use of supervised deep learning for the analysis of galaxy images, such as convolutional neural networks (CNN), has proven to be extremely successful for classifying galaxy images (e.g, Dieleman, Willett & Dambre 2015; Huertas-Company et al. 2015; Cheng et al. 2020; Ghosh et al. 2020; Hausen & Robertson 2020; Vega-Ferrero et al. 2021; Domínguez Sánchez et al. 2022; Walmsley et al. 2022), including classifications of relatively rare objects such as strong lensed galaxies (Lanusse et al. 2018; Cheng et al. 2020) or post-mergers (e.g. Bickley et al. 2021). However, one of the main drawbacks of supervised learning approaches is the need for a large sample of labelled galaxies (of the order of thousands) to train and test the algorithm and its performance in different regimes (see Huertas-Company & Lanusse 2022 for a review on the topic). An alternative is the use of simulations: the viability of using galaxies from hydrodynamical simulations to train deep learning models to classify real galaxies and mergers has indeed been shown in Bottrell et al. (2019b) and Huertas-Company et al. (2019). The scarcity of a large number of galaxies showing tidal features to be used as training data has prevented to develop automated supervised detection algorithms, and so far there have been almost no attempts in the literature to this respect. A pioneering effort to develop a CNN for tidal stream detection was presented in Walmsley et al. (2019), where the authors used imaging for the Canada–France–Hawaii Telescope Legacy Survey-Wide Survey (Gwyn 2012). However, the models only achieved a 76 per cent accuracy, probably due to the small size of the training sample (~1700 galaxies, of which only 305 showed tidal stream detections).

In this work, we use synthetic HSC images of galaxies generated by the NewHorizon cosmological simulations (Dubois et al. 2021) to examine the viability of using CNNs to identify galaxies with tidal features. The original sample, described in Section 2, includes ~6000 images at different surface brightness limits classified by professional astronomers. This is the largest catalogue of tidal features based on visual classification up to date. We describe our CNN and training strategy in Section 3, and test the ability of the CNNs to recover human-like classifications in Section 4, where we present the performance of the model as a function of the feature class (Section 4.1), redshift (Section 4.2), and image depth (Section 4.3). The outcome of applying the models to real data are discussed in Section 5, including an attempt of using the Kado-Fong et al. (2018) classification as a training sample. We summarize our results and discuss their implications in Section 6.

2 DATA

We take advantage of the galaxy images and labelling presented in Martin et al. (2022, herafter M22). The galaxies are gener-
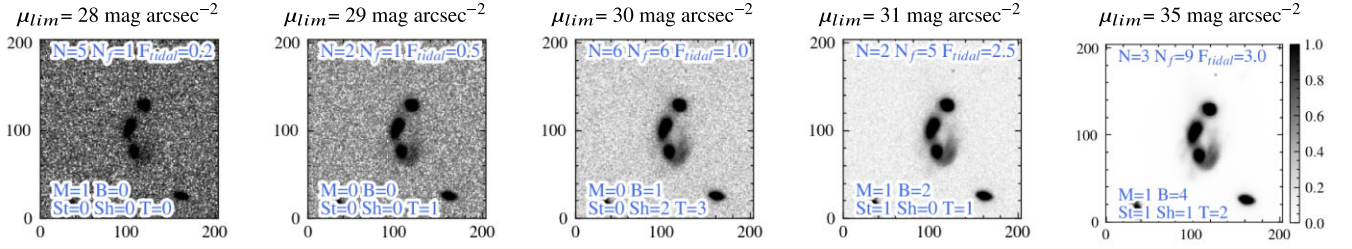
Figure 1. Example of the classification performed in M22. Images of the same galaxy observed at $z = 0.05$ with different μ_{lim} (28, 29, 30, 31, 35 mag arcsec^{-2}, form left to right) were classified by a varying number of astronomers (N) into different categories. The number of observed features of each class is reported in the cut-outs (St = streams, Sh = shells, T = tails, M = mergers, B = bridges) along with the total number of features (N_f) and $F_{Tidal} = N_f/N$. In this work, we consider as positive examples to those images with $F_{Tidal} > 1$, negative those with $F_{Tidal} = 0$, and uncertain otherwise. Following this criteria, the images with $\mu_{lim} = 28$ and 29 have an uncertain classification, while those with $\mu_{lim} > 29$ are classified as showing tidal features. The cut-outs are normalized in the (0, 1) range using *arcsinh stretch*, as described in Section 3.1.

ated with NewHorizon, state-of-the-art cosmological hydrodynamical simulations (Dubois et al. 2021), a zoom-in of the parent Horizon-AGN simulation (Dubois et al. 2014). NewHorizon combines high-stellar mass ($1.3 \times 10^4 \, M_\odot$), and spatial resolution ($\sim$34 pc) with a contiguous volume of $(16 \, \text{Mpc})^3$. Given the diffuse nature of galaxy stellar haloes, the trade-off between resolution and volume is an important consideration. The simulations adopt the cosmological parameters from Komatsu et al. (2011), $\Omega_m = 0.272$, $\Omega_\Lambda = 0.728$, $\Omega_b = 0.045$, $H_0 = 70.4 \, \text{km s}^{-1} \, \text{Mpc}^{-1}$). We refer the reader to M22 for more technical details on the simulations.

2.1 Mock galaxy images

The parent sample consists of 36 unique galaxies, with masses above $10^{9.5} \, M_\odot$ at $z = 0.2$, and their progenitors at $z = 0.4$, 0.6, and 0.8. Realistic HSC-like mock images are generated by convolving the smoothed star-particle fluxes with the *g*-band HSC 1D PSF (Montes et al. 2021). Three projections of each snapshot (*xy*, *xz*, *yz*) are created at five different distances (corresponding at $z = 0.05$, 0.1, 0.2, 0.4, and 0.8). The physical field of view is 100 kpc (proper) cropped from the initial 1 Mpc cube. Mock images are produced for each galaxy by extracting star particles centred around each galaxy. The spectral energy distribution (SED) for each star particle is then calculated from a grid of Bruzual & Charlot (2003) simple stellar population models assuming a Salpeter (1955) IMF. They account for dust attenuation of the SEDs using a screen model in front of each particle for which a gas-to-dust ratio of 0.4 Draine et al. (2007), and a Weingartner & Draine (2001) $R = 3.1$ Milky Way dust grain model are assumed. After redshifting each particle SED, the flux of each particle is calculated by convolving with the appropriate bandpass transmission function. Finally, random Gaussian noise is added to the simulated images to reach different limiting surface brightness μ_r^{lim} corresponding to 28, 29, 30, 31, and 35 mag arcsec^{-2} (3σ, 10×10 arcsec). The combination of these parameters results in 10 800 unique simulated images. Since the pixel angular size is fixed, the difference in distance of the galaxies directly translates into cut-outs of different sizes (26×26, 36×36, 60×60, 108×108, 204×204 pixels, from $z = 0.8$ to 0.05). In order to increase the sample size and to have mock images which resemble current observations better, we have generated 2×1453 additional snapshots with $\mu_{lim} = 26$ and 27 mag arcsec^{-2} by adding Gaussian noise following equation (3) from M22 to the deepest available image of each particular counterpart (i.e. with the corresponding ID, snapshot, redshift, and projection).

2.2 Tidal feature classification

M22 performed a visual inspection of $\sim$8000[1] unique images by 45 expert classifiers, with a random subset of them classified six times by identifying the presence of tidal features and classifying them into stellar *streams, tidal tails, shells, tidal bridges, merger remnants, double nuclei*, or *miscelanea*.[2] The classification was summarized in a catalogue including 5 835 unique images. The missing images were not included in the classification catalogue for being too noisy. We use this catalogue as parent sample in our work. The visually classified images were created at HSC pixel angular scale of 0.2 arcsec, but rescaled to 1 arcsec, comparable to the FWHM of the PSF used (an observer might reasonably rebin like this in order to gain additional depth without losing any detail). This rebinning will have a significant impact when applying the models trained with these images to real HSC-SSP data, as we discuss in Section 5. In this work, we use the exact same images as those visually classified to train the deep learning algorithm, so that the labels are consistent.

Fig. 1 shows the result of the classification for a particular galaxy image observed at redshift $z = 0.05$ with different limiting surface brightness. Each image is classified by a number of astronomers (N), which assign the number of observed features (N_f) of each class to the image. This means that more than one class can be assigned to each image and that the classification can change with μ_{lim}, but also due to projection effects or spatial resolution (redshift). For this particular example, the deepest image ($\mu_{lim} = 35$ mag arcsec^{-2}) was classified by $N = 3$ astronomers, which annotated features of *streams, shells, tidal tails, merger*, and *bridges* adding up to a total of $N_f = 9$. On the other hand, the shallower image ($\mu_{lim} = 28$ mag arcsec^{-2}) was classified by $N = 5$ astronomers, of whom only one annotated the feature class of *merger* ($N_f = 1$).

To the best of our knowledge, this is the sample with the largest number of tidal detections visually classified by professional astronomers up to date, making it the optimal sample for training a deep learning algorithm for automated detection of tidal features. However, the example from Fig. 1 illustrates the challenges of the visual identification of tidal features: the definition of the different classes of features is not objective, and there is a discrepancy between

---

[1]Note that this number is smaller than 10 800 quoted on Section 2.1 due to missing progenitors at some snapshots, which are too small to be detected by the structure finder at higher redshift.

[2]The *plume* and *asymmetric* categories described in M22 are combined into a single *miscelanea* category in the catalogue, since there was a large degree of overlap between the two.
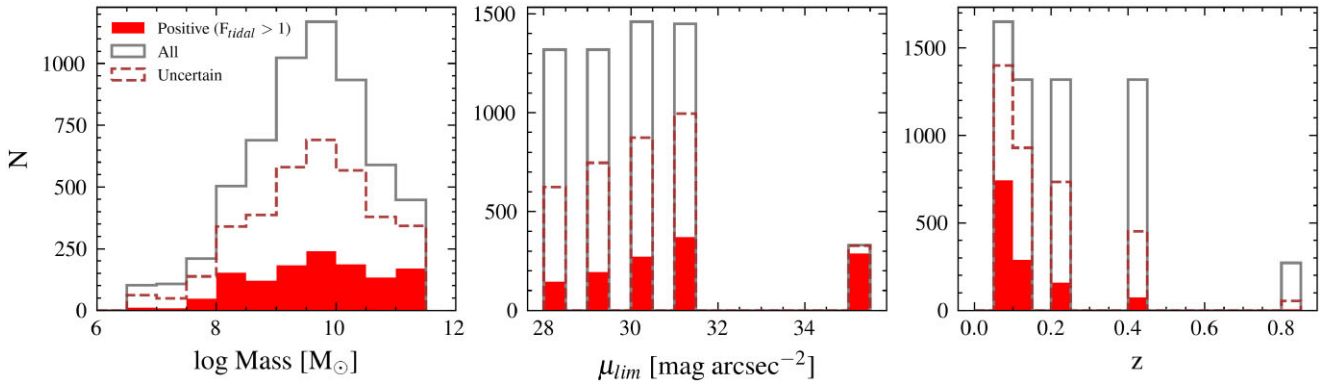
Figure 2. Distribution of stellar mass (left), limiting surface brightness (middle), and redshift (right) of the images from the parent sample presented in M22. The grey empty histograms represent the full sample (5835 images), the red filled histograms show the images labelled as positive examples of tidal features (i.e. with $F_{Tidal} > 1$), and the brown empty histograms correspond to images with uncertain classifications ($0 < F_{Tidal} < 1$ or labelled as *misc/double nucleus* only). Note the large dependence of the fraction of tidal feature identification by the astronomers with surface brightness limit and redshift (or, equivalently, cut-out size).

the classifiers. In some cases, the same images are classified as showing tidal features by some classifiers and as featureless by others. This is a warning about the reliability of the visual classifications, and how much they should be trusted as the ground truth. Although, we are well aware of these caveats, we continue to use this data set in our analysis as is the largest and most complete galaxy sample with tidal feature labels up to date.

To simplify the problem in this work, we focus on the identification of the presence (or not) of a tidal feature, regardless of its category and, thus, we consider all the tidal feature classes simultaneously. Since the images were classified by a varying number of experts, ranging from one to six, and more than one tidal feature category could be assigned to each image, we divide the number of tidal feature identifications by the number of classifiers. We refer to this quantity as the *fraction of tidal detections, $F_{Tidal} = N_f/N$*, and consider certain classifications those with $F_{Tidal} = 0$ or ≥ 1 (corresponding to 39 and 38 per cent of the sample, respectively). For the images with $0 < F_{Tidal} < 1$ (the remaining 22 per cent), the classification of different experts were inconsistent, and we refer to these cases as uncertain classifications. To avoid including uncertain classifications in the loop, we remove the images with $0 < F_{Tidal} < 1$ from the train and test samples. After visual inspection of some images, we found that the classes *misc* and *double nucleus* do not fit exactly into the tidal features we are aiming to detect. Therefore, images classified *only* as *misc* or *double nucleus* are also removed from the analysis.

The distribution in mass, surface brightness limit, and redshift of the parent sample, and the images classified as showing tidal features are shown in Fig. 2. The detection of tidal features by humans is largely dependent on the depth of the images and on the image size (or redshift of the galaxy), as reported by M22 and clearly seen in Fig. 2. This has important consequences for the performance of the algorithm for automated detection of tidal features, as we discuss in Section 4.

3 METHODOLOGY

We use supervised learning for the identification of galaxies showing tidal features; i.e. we need to provide the algorithm with the ground truth we would like to recover in the form of labels (in this case, tidal feature detection or not). We use CNNs, a class of artificial neural networks consisting of convolution kernels that slide along input features and provide feature maps. These maps are then passed through a fully connected network that outputs a value, corresponding to a particular property that we want to learn. The final function (or weights of the model) is the one that minimizes the difference between the output and the input labels. In this work, the input to the CNN are single-band images in the HSC *r*-band (we use the *r*-band images since these were the images classified by the professional astronomers in M22) with their corresponding labels (0s for non-tidal detections and 1s for tidal features). The output of the model, P_{Tidal}, is the probability that the image shows a tidal feature.

3.1 Image pre-processing

Before being fed to the CNN, the galaxy images are normalized in the range (0, 1) to avoid operating with very large numbers. For the normalization, the commonly used *asinh stretch* function [3] (see Lupton et al. 2004) is used, combined with a sigma clipping of 3 per cent of the faintest and the brightest pixels of each image. This pre-processing enhances the detection of low surface brightness features. The images are converted to the same size, 69 × 69, (the input to the CNN is an array of fixed dimensions) by rebinning or interpolating the pixel flux, depending on the original image size. We tested input sizes of 100 × 100 without obtaining significant changes in the results. Throughout the paper, we use the 69 × 69 stamps as reference.

3.2 Input labels

We use a binary classification to separate images which show tidal features (positive samples, labelled as 1s) from images without tidal signatures (negatives, labelled as 0s). Therefore, we unify all classes of tidal features into a single one (detections or non-detections). As explained in Section 2.2, we use the quantity F_{Tidal} to select positive and negative examples, and leave out of the analysis images with uncertain classifications.

For the images generated specifically for this work at $\mu_{lim} = 26$, 27 mag arcsec^{-2}, we do not have classifications by the professional astronomers as these images were not part of the original M22 sample. We choose to use the labels of their counterpart images

---

[3]https://docs.astropy.org/en/stable/api/astropy.visualization.AsinhStretch.html

Table 1. Architecture of the CNN used in the main text.

Layer type	Output shape	Parameters
Input	(69, 69, 1)	0
Conv2D	(69, 69, 32)	320
MaxPooling2D	(34, 34, 32)	0
Conv2D	(34, 34, 48)	13 872
MaxPooling2D	(17, 17, 48)	0
Conv2D	(17, 17, 64)	12 352
MaxPooling2D	(8, 8, 64)	0
Flatten	(4 096)	0
Dense	(64)	262 208
Dense	(1)	65
Total number of parameters	–	288 817

(i.e. with the same galaxy ID, snapshot, redshift and projection) at $\mu_{lim} = 28 \, \mathrm{mag \, arcsec^{-2}}$ as their 'ground truth' label. This exercise allows us to test whether or not the algorithm can recover visually classified features in images with surface brightness limit $2 \, \mathrm{mag \, arcsec^{-2}}$ shallower than the images used for their visual classification.

We randomly split the sample in 85 per cent for training (resulting in 4418 images, out of which 1539 are tidal detections), and reserve 15 per cent for testing (820, out of which 223 are tidals).

3.3 CNN architecture

The CNN architecture discussed in the main text, based on the one presented in Walmsley et al. (2019), is summarized in Table 1. It consists on three 2D convolution layers with 32, 48, and 64 filters with sizes 3, 3, and 2, respectively, and 2×2 *max-pooling* windows. They are followed by a fully connected layer with 64 neurons, Rectified Linear Unit (ReLU) non-linear activation function and 0.5 dropout rate. A final single neuron outputs values converted to the (0, 1) range by applying a sigmoid function. Binary-crossentropy is used as loss function and Adam as optimizer. The number of free parameters of this CNN is 288 817 (for input sizes $69 \times 69 \times 1$).

We have tested other CNN architectures, namely the one commonly used by the authors (e.g. Domínguez Sánchez et al. 2018 and Domínguez Sánchez et al. 2022), consisting on four 2D convolutional layers with 32, 64, 128, and 128 filters with sizes 6, 5, 2 and 3, 2×2 *max-pooling*, and 0.25 dropout,[4] followed by a fully connected layer with 64 neurons and 0.25 dropout. The number of free parameters is 2 600 545, almost ten times larger than in the Walmsley et al. (2019) CNN. A variation of the Domínguez Sánchez et al. (2018) architecture, with filter sizes (3, 3, 2, 3), and adding a fully connected layer with 16 neurons before the final layer, has also been tested. In addition, conventional networks such as ResNet-18, -50, -101 (He et al. 2016) and EfficientNet-B0,-B1, -B4, and -B7 (Tan & Le 2019) have been attempted. As the use of more complicated CNNs did not significantly improve the results, we have decided to use the Walmsley et al. (2019) architecture as a reference due to its simplicity with respect to other algorithms.

We use an overall standard strategy for training. We train for 100 epochs with a batch size of 100 and a validation split of 0.2 (from the training sample). Data augmentations are performed while training, including vertical and horizontal flip, weight, and height shifts (by 0.05 per cent), zoom-in and out (0.75–1.3) and

[4]This is a slight modification with respect to the original configuration.

rotations (0°, 90°, 180°, 270°). We train 10 independent models, randomly changing the initialization weights and the training and validation sets. During the training, we observed no signs of over-fitting. The results presented in the following sections are based on the average of the output of the 10 models, which we refer to as P_{Tidal}.

4 RESULTS

In this section, we study the performance of our models when applied to the test data set. We consider two different tests sets: the one containing only the original simulations and labels by professional astronomers (i.e. surface brightness $\mu_{lim} \geq 28 \, \mathrm{mag \, arcsec^{-2}}$), and the test set which includes the original and the simulated images at $\mu_{lim} = 26, 27 \, \mathrm{mag \, arcsec^{-2}}$. We will refer to the former as the *original* test sample and to the latter as the *original + shallow* test sample.

We use standard metrics for studying the performance of the models:

$$\text{Accuracy} = \frac{\text{TP} + \text{TN}}{\text{TP} + \text{TN} + \text{FP} + \text{FN}} = \frac{\text{TP} + \text{TN}}{\text{Total}} \quad (1)$$

$$\text{Precision} = \frac{\text{TP}}{(\text{TP} + \text{FP})} = \frac{\text{TP}}{P_{pred.}} \quad (2)$$

$$\text{Recall} = \frac{\text{TP}}{(\text{TP} + \text{FN})} = \frac{\text{TP}}{P_{input}} \quad (3)$$

$$\text{F1} = 2 \times \frac{P \times R}{(P + R)}, \quad (4)$$

where TP, TN, FP, and FN stand for true positives, true negatives, false positive and false negative, respectively, while P_{pred} and P_{input} are the total number of predicted and input positives, respectively. To separate the instances into positive and negative predictions, we use the *binary classification threshold probability*, P_{th}, which is the value that optimizes the true positive rate (TPR, i.e. the fraction of correctly identified tidal detections) and the false positive rate (FPR, i.e. the fraction of non tidals classified as tidal detections) simultaneously. The number of galaxies in each test sample and the fraction of positives (labelled as tidal detections in the input catalogue), as well as the accuracy, precision, recall, and F1 score of each sample is reported in Table 2. The accuracy is the fraction of correctly classified instances, the precision is the fraction of TP among the instances classified as positive (analogue to the purity), while the recall is the fraction of TP among the positive input instances (analogue to the completeness). Finally, the F1 score is the harmonic mean of the two.

Fig. 3 shows the receiver operating characteristic curve (ROC) that represents TPR versus FPR as the discrimination threshold (P_{th}) is varied. An adequate classifier would maximize the TPR while keeping the FPR low. The area under the ROC curve (AUC) is above 0.9 in both cases (a perfect classifier would have AUC = 1). We also show the confusion matrices for the two test samples using as probability threshold the optimal value for each sample to separate the predictions into positive and negative classes. As reported in Table 2, the accuracy (equation 1) for the *original* and *original + shallow* test samples is 0.84 and 0.85, while the precision (or purity, equation 2) is 0.72 and 0.71, respectively. These values are surprisingly similar, taking into account the inclusion of ∼300 images with $\mu_{lim} < 28$ in the *original + shallow* test sample for which the ground truth is assumed to be the labels at $\mu_{lim} = 28$, i.e. those reported for images two magnitude deeper than the actually classified images. The main difference is in the recall (or completeness, equation 3) that drops from 0.85 for the *original*

Table 2. Number of galaxies in the *original* and *original + shallow* test samples, and the fraction of those labelled as tidal features, as well as the accuracy, precision, recall, and F1 score obtained when selecting as positive predictions the images with model scores above their corresponding P_{th}.

Test sample	N_{test}	Positives (per cent)	P_{th}	Accuracy	Precision	Recall	F1
Original	532	33	0.32	0.84	0.72	0.85	0.78
Original + shallow	820	27	0.31	0.85	0.71	0.75	0.73
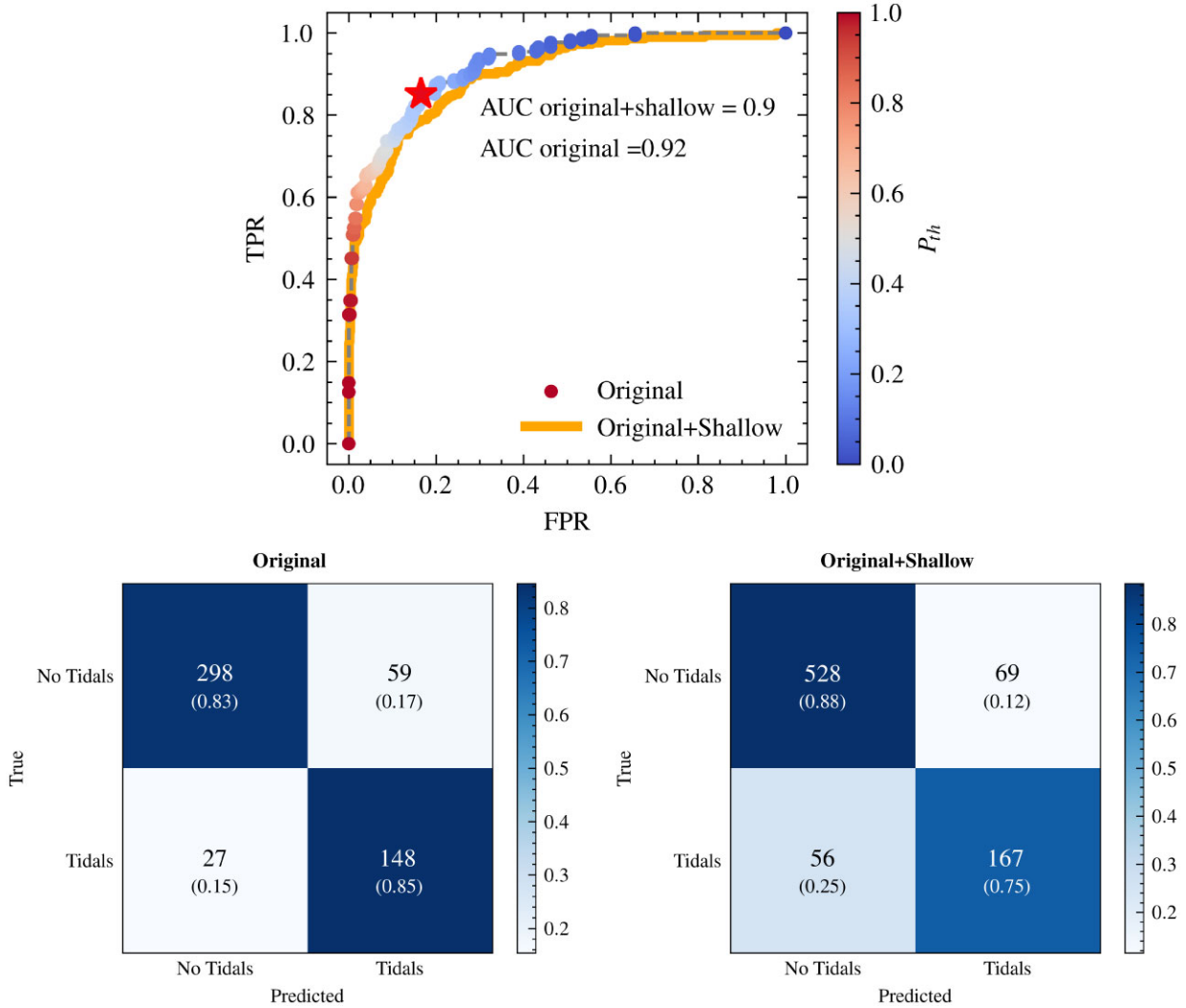
Figure 3. *Upper panel:* ROC curve – True Positive Rate as a function of False Positive Rate – for the *original* (circles, coloured coded by P_{th}) and *original + shallow* (orange line) test samples. The red star marks the optimal threshold for the *original* sample. *Bottom panels:* Confusion Matrix for the *original* (left) and *original + shallow* test sample (right) obtained when selecting positive samples as those above the corresponding P_{th} of each sample. Input labels are shown in the *y*-axis, predictions in the *x*-axis. The number of objects is reported in each quadrant, colour coded by the fraction of that particular true class (also shown in parenthesis).

test sample to and 0.75 for the *original + shallow* test sample. As expected, it is more difficult for the algorithm to recover tidal detections in shallower images. We discuss the surface brightness dependence of the classification in Section 4.3. Since the precision values are very similar for the two test samples, but recall is smaller for the *original + shallow* test sample, the F1 score (equation 4) is also lower for the *original + shallow* (F1 = 0.73) than for the *original* sample (F1 = 0.78).

4.1 Dependence on tidal feature class

Now we study the ability of our CNN to detect different classes of tidal features. Fig. 4 shows the output probability of our model, P_{tidal} (larger values correspond to more confident detection of tidal features), divided in the classes provided in the M22 catalogue. Clearly, there are classes which are easier to identify than others. For example, all the *shells* in the test sample are recovered, and the TPR for the *streams* is 0.84, while for *mergers* or *tidal tails* is below
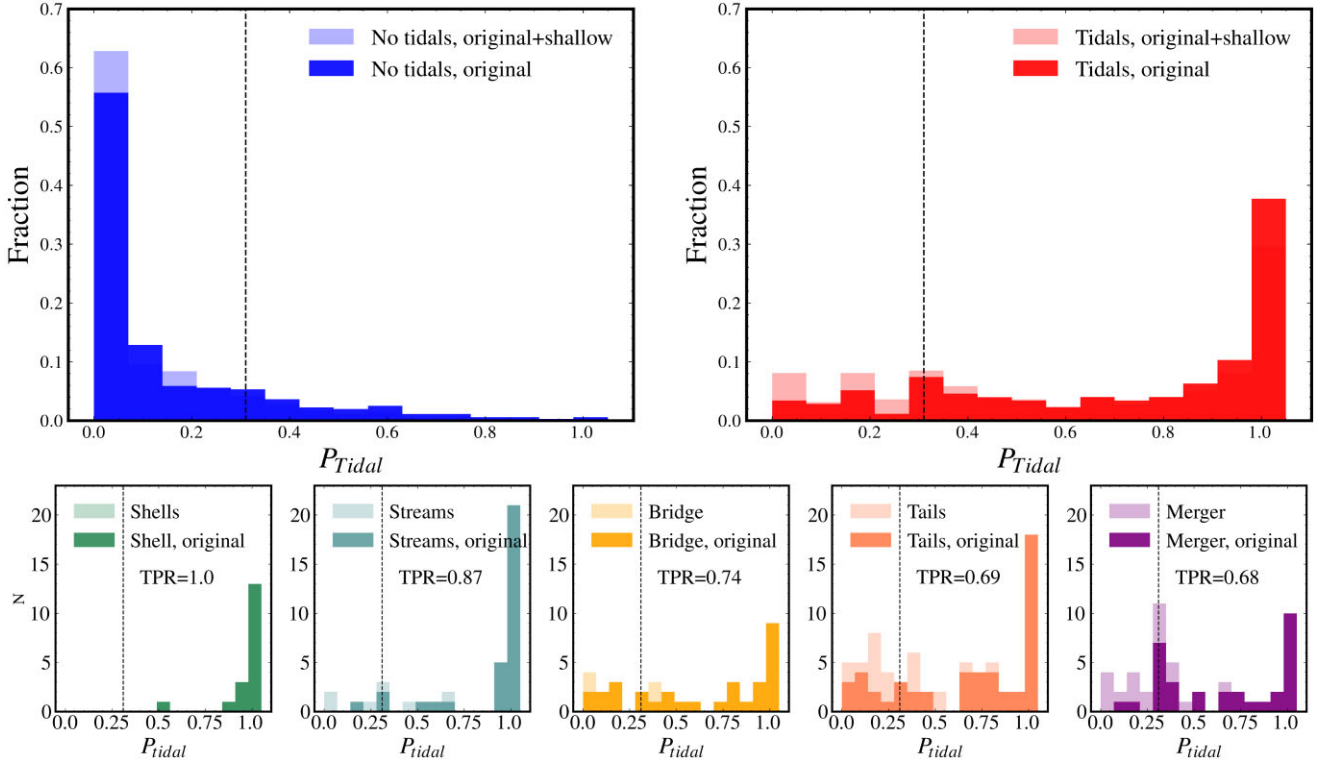
Figure 4. *Upper panels:* Output probability distribution of the model for tidal detection, P_{Tidal}, for the test sample divided into non-tidal visual classifications (left-hand panel, blue) and tidal visual classifications (right-hand panel, red). Darker colours represent the *original* sample, lighter colours the *shallow* sample. *Lower panels:* P_{Tidal}, for the test sample divided into different categories, as stated in the legend. The dashed line is $P_{\text{th}} = 0.31$, the threshold used to define an instance as positive or negative. The true positive rate (TPR) of each category for the *original + shallow* sample is reported in the corresponding panel.

0.7. It is also evident from Fig. 4 that the model performs worse for the *shallow* sample: the P_{tidal} values are lower for the positive cases of this subsample. We discuss in more detail the effect of the μ_{lim} in Section 4.3.

Fig. 5 shows representative examples of TP identifications of *shells, streams,* and *mergers* at different surface brightness limits. The features are very evident for the deep images (right-hand panels), and, in some cases, it is surprising that the model is able to identify the tidal features in the more noisy images (left-hand panels). Besides, the cut-outs are displayed at their original size, not binned to 69×69, which is the input to the CNN. These examples show that *shells* and *streams* are easier to identify by eye than *mergers*. We note, however, that the number of *shells* in the test sample is small (12), and that there are no *shells* in the *shallow* test sample. This is due to the fact that there are no visually identified *shells* in images shallower than $\mu_{\text{lim}} = 28$ mag arcsec^{-2}, from which the labels for the *shallow* sample come from. In other words, the fact that we are recovering more *shells* may be due to these structures being identified by eye only in the deeper images. We note again that the different classes reported in the M22 catalogue are not mutually exclusive (see also Fig. 1), and therefore images identified as *shells* can also fall into other categories (this happens indeed for 10 out of 12 *shells* in the test sample).

FN cases are shown in Fig. 6 for *streams* and *mergers*. As all the *shells* in the test sample are correctly identified by our model, there are no FN for this category. Even for the deeper images (right-hand panels), it is difficult to identify the tidal features, while the shallower images (left-hand panels) are dominated by noise. Therefore, it is not surprising that the model fails in these cases.
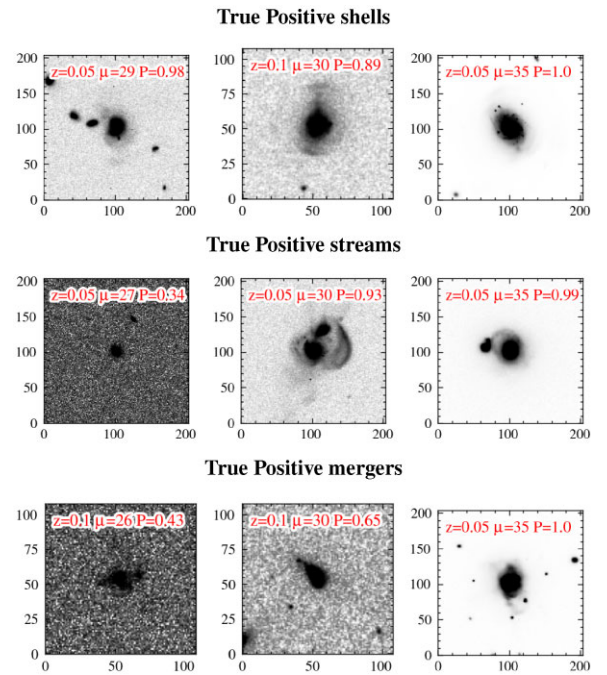

Figure 5. TP examples of shells, streams, and mergers, from top to bottom. The cut-outs have been processed as described in Section 3.1, but are shown at their original sizes (i.e. they are not binned to 69×69, which is the input to the CNN), and the *x* and *y* axes correspond to the number of pixels. The information shown in each cut-out corresponds to the redshift, the surface brightness limit (increasing from left to right), and the output probability of the model, P_{Tidal}.
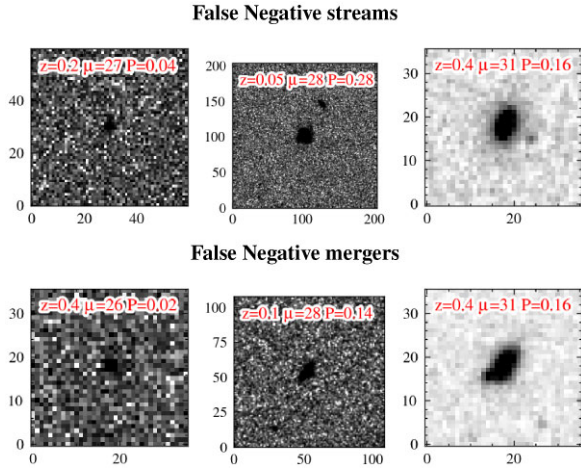
Figure 6. Same as Fig. 5 but for FN examples of *streams* and *mergers* (top and bottom panels, respectively). Note that there are no false negative shells (see Fig. 4). The features are hard to detect by eye, so it is not surprising that the model fails in these cases.
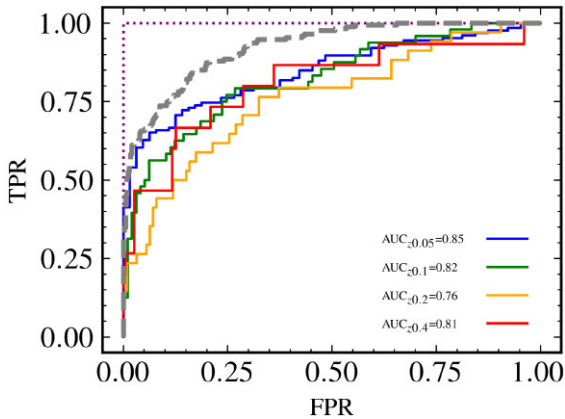

Figure 7. ROC curves for galaxies at different redshifts, colour coded as indicated by the legend. The grey dashed line shows the ROC curve for the full *original* sample. Note that there are no positive cases at $z = 0.8$, and the model correctly classifies all the images at this z as negatives; hence we represent the ROC curve as the dotted purple line.

4.2 Dependence with redshift

In this section, we report the performance of the model when the test sample is divided into different redshift bins, which is directly related to the original stamp size (the stamps are then resampled into 69 × 69 because the input to the CNN has fixed dimensions, see details in Sections 2 and 3.1). Fig. 7 shows the ROC curves as a function of redshift. As expected, the larger AUC is obtained in the lower redshift bin ($z = 0.05$). However, the dependence on redshift is not very strong and not even linear. For example, the AUC is larger for $z = 0.4$ (AUC = 0.81) than for $z = 0.2$ (AUC = 0.76), probably due to the lower fraction of visual detections at higher redshifts, which increases the overall accuracy. This is evident for $z = 0.8$ (shown as a dotted line), where there are no galaxies classified as tidal detections in the test sample, neither in the input labels nor by our model, and therefore the accuracy is 100 per cent.
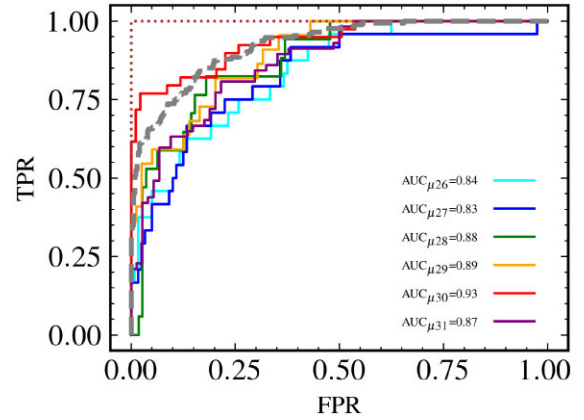
Figure 8. Same as Fig. 7 for images at different surface brightness, colour coded according to the legend. Note that at $\mu = 35$ mag arcsec^{-2} all images show tidal features and are correctly classified as such by our model (we plot the ROC curve as the brown dotted line).

4.3 Dependence with surface brightness

Finally, we study the dependence of the model performance on the surface brightness of the images to be classified. Fig. 8 shows the ROC curve for the different μ_{lim} values. The lower AUC correspond to the shallower images ($\mu = 26, 27$), as expected, and the best results are obtained for $\mu = 30$ mag arcsec^{-2}. We show the ROC curve for $\mu = 35$ mag arcsec^{-2} as dotted line because all the images from the test sample are classified as tidal detections, both in the input catalogue and by the model (just the opposite of what happens at $z = 0.8$). Surprisingly, the AUC at $\mu = 31$ mag arcsec^{-2} is lower (AUC = 0.87) than at $\mu = 30$ mag arcsec^{-2} (AUC = 0.93), and comparable to the values obtained at $\mu = 28$ mag arcsec^{-2}.

To shed more light on the classification efficiency, Fig. 9 shows the confusion matrices (generated by setting $P_{th} = 0.31$) for three surface brightness limits ($\mu = 26, 30, 31$ mag arcsec^{-2}). These confusion matrices highlight the fact that the large AUC for $\mu = 26$ mag arcsec^{-2} is mainly driven by the ability of the classifier to correctly identify images without tidal detections (98 per cent accuracy for the negative subsample), while it struggles to correctly classify the tidal detections (only 33 per cent are recovered in this surface brightness range). On the other hand, at $\mu = 31$ mag arcsec^{-2}, the contrary happens: the model is able to correctly identify 89 per cent of the tidal detections, at the cost of misclasifying 35 per cent of the non-detections. At $\mu = 30$ mag arcsec^{-2}, the model is able to correctly identify 90 per cent of the tidal detections while keeping the contamination (i.e. the number of FP) at 26 per cent.

While this trend could be expected, and is in line with the larger fraction of tidal detections obtained in deeper images by visual inspection (see Fig. 2), it could be an indication that our model has, at least to some extent, learned the signal-to-noise of the images: it tends to classify deeper images more frequently as tidal detections. To test this assumption, Fig. 10 shows the accuracy, precision, and recall for each surface brightness bin, as well as the fraction of positive samples (tidal detections) in the input catalogue.

As reflected by the confusion matrices, the recall (completeness) of the model is highly dependent on the depth of the images to be classified, going from around $R \sim 0.40$ at $\mu = 26$ mag arcsec^{-2} to $R \sim 0.90$ at $\mu = 31$ mag arcsec^{-2}. However, this is not as clearly reflected in the precision (purity) values, roughly constant and above $P \sim 0.60$ at all surface brightness. In the same way, the accuracy is stable throughout the whole magnitude range (∼80 per cent), indicating
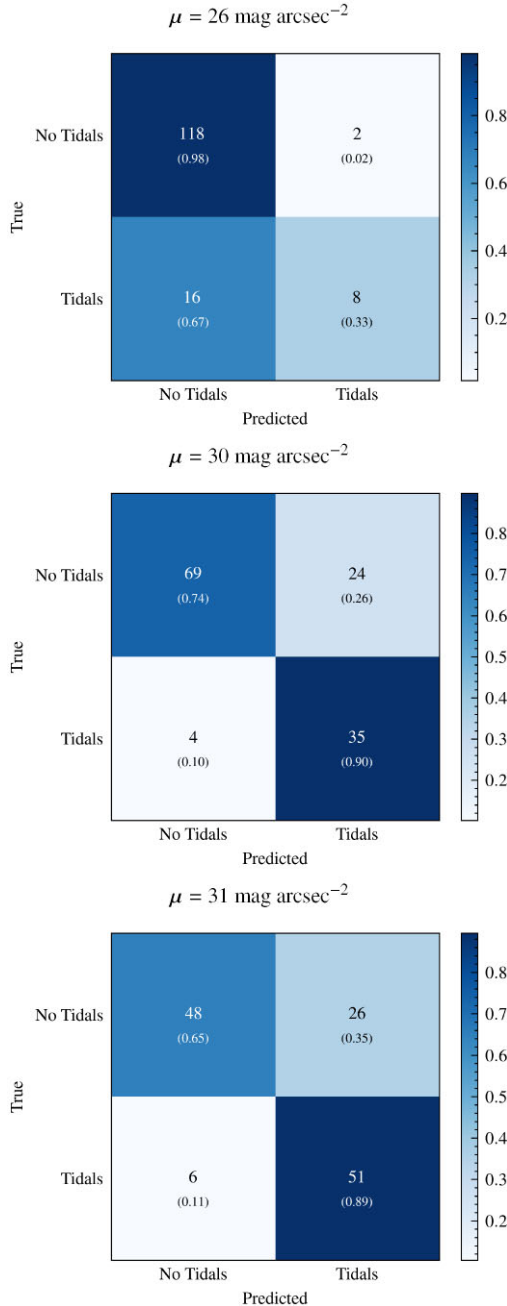
$\mu = 26 \text{ mag arcsec}^{-2}$

$\mu = 30 \text{ mag arcsec}^{-2}$

$\mu = 31 \text{ mag arcsec}^{-2}$

Figure 9. Confusion matrices for three different surface brightness bins: $\mu_{\text{lim}} = 26, 30, 31 \text{ mag arcsec}^{-2}$, from top to bottom. The number of objects is reported in each quadrant, colour coded by the fraction of that particular true class (also shown in parenthesis).

that the model has not simply learned the signal-to-noise of the images. The fact that the accuracy does not improve with μ_{lim}, even if the recall (completness) does, can be explained by a larger fraction of FP. However, the increase in FP does not decrease the precission (purity) because of the larger fraction of tidal detections in the input catalogue at higher μ_{lim} (black symbols in Fig. 10), which together with the larger recall increase the number of TP to counterbalance the larger number of FP.

We would like to highlight here again that the labels used for the *shallow* sample ($\mu_{\text{lim}} < 28 \text{ mag arcsec}^{-2}$) correspond to the visual classification of the images with $\mu = 28 \text{ mag arcsec}^{-2}$, which
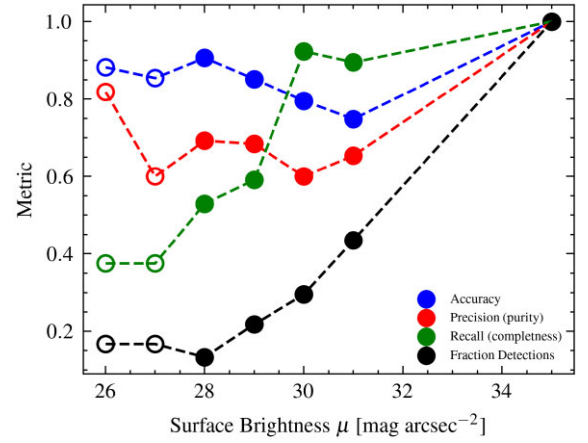

Figure 10. Accuracy (blue), precision (red), and recall (green) obtained for the test sample as a function of the images' surface brightness μ_{lim}. The fraction of tidal detections in the input catalogue is shown in black. The bins at $\mu_{\text{lim}} = 26, 27 \text{ mag arcsec}^{-2}$ are plotted as empty circles to highlight the fact that they are not part of the original sample from M22; the labels used for training and testing are the ones for their corresponding images at $\mu = 28 \text{ mag arcsec}^{-2}$.

explains the drop in completeness in this surface brightness regime. Indeed, it is remarkable that our model is able to recover 40 per cent of the images with tidal detections, even when the images are two orders of magnitude shallower that the ones used for labelling. This is in agreement with recent results suggesting that CNNs trained with 'intrinsic' ground truth can recover astronomical features hidden to the human eye (see e.g. Vega-Ferrero et al. 2021). This result could have a large impact on the design strategy of future surveys.

We emphasize that redshift and surface brightness limits are intertwined in the current analysis. Unfortunately, the test sample size is too small to examine the trends at each μ_{lim} limit separately, at fixed redshift (or viceversa).

5 APPLICATION TO REAL HSC-SSP DATA

Our models are trained in HSC-like mock images. Therefore, it is important to test the performance of the algorithm in real data with similar characteristics to the training data set. We thus use images from the HSC-SSP survey (Hyper Suprime-Cam Subaru Strategic Survey) Wide layer Aihara et al. 2018a, b. The HSC Wide layer covers the largest on-sky area at a relatively shallow depth ($i \sim 26$) relative to the Deep and UltraDeep Layers ($i \sim 27$ and 28, respectively).

In particular, we have applied our models to the HSC-SSP images presented in Kado-Fong et al. (2018). These are $\sim 21\,000$ galaxies from the internal data release S16A, with spectroscopic redshifts from SDSS at $0.05 < z < 0.45$. Kado-Fong et al. (2018) used a filtering algorithm to identify tidal features, combined with visual classification of the features detected by such filtering, resulting in a sample of ~ 1200 tidal feature detections. Our first approach to this work was to use the labels from Kado-Fong et al. (2018) sample to train the algorithm for tidal stream identification, but after exhaustive testing, the results were not good enough (F1 = 0.37), mostly due to the small completeness achieved by the models ($R = 0.26$).

As previously explored in the context of tidal feature classification of mock images (Section 2.2), one source of significant label noise is the reliability of visual inspection itself. Visual inspection of the full sample by three professional astronomers (I.D., H.S., O.K.L.)

provided a new classification, which revealed that only 1/4 of the galaxies showing tidal features according to the filtering algorithm were classified as such by all visual classifiers. We believe that the combination of noisy labels, small positive training sample, and low surface brightness features to be detected limited the performance of the algorithm. This was the main reason why we decided to use the HSC-like mock images for training the CNN. We note that the original classification by Kado-Fong et al. (2018) used both the images and the output of the filtering algorithm in order to detect features close to the host galaxy, so it is expected that the re-classification of the images alone would yield a lower tidal feature detection rate. On the other hand, as the original Kado-Fong et al. (2018) sample focused on the comparison of the properties of stream and shell hosts, the visual inspection was performed only for the images, where a tidal detection was identified by their filtering algorithm, meaning that the completeness of the sample is uncertain.

It is well known that deep learning models are sensitive to the characteristics of the training sample, and these techniques such as transfer learning (e.g. Domínguez Sánchez et al. 2019) should be used for optimizing models trained on different data sets than the target sample. We attempted, without success, to use transfer learning to fine tune the models on real HSC-data, making exhaustive tests on the number of layers to be trained, the learning rate, etc. The best result we obtained is AUC = 0.64, and the output values are concentrated towards the lower end ($P_{Tidal} < 0.7$). These poor results emphasize the strong dependence of the model performance on the data they are trained with and warns us against carelessly applying models to different data domains. It also suggest that mock images from simulations are not as realistic as we might have expected.

A possible explanation for the bad performance could be the differences in the way the mock images were created compared to real HSC data. For example, the angular resolution of the HSC-mock images is poorer (1 arcsec versus 0.″167 for real HSC-SSP). In addition, the simulated images do not include real backgrounds, processing artifacts, contaminating sources, or sky subtraction residuals. This may compromise the model's ability to assess real data, as already discussed in Bottrell et al. (2019a). The morphological classification of TNG simulated images presented in Huertas-Company et al. (2019) was significantly improved by adding realism to the simulated images. Unfortunately, adding realism to the images could change the visual classification used as 'ground truth': some features could become undetectable in the presence of brighter objects. Therefore, training the CNN, with more realistic mock images and new labels, is beyond the scope of the current analysis. We will investigate these possible improvements in the forthcoming studies.

The reason why transfer learning might not solve the domain shift could be the fact that the μ_{lim} in the simulated images is not fixed. This implies that the model needs to transfer from many sparsely sampled domains to another, instead of transferring from one well-sampled domain to another. Intuitively, the former may be harder. Another aspect which could have a significant effect is the small parent sample of galaxies used to produce the simulations, based on 36 galaxies only that may not represent the diversity of real galaxy populations. Since the observed sample is flux limited and the simulated sample is volume limited, the former should have a flatter mass distribution with more massive galaxies. Also, the real data have continuous redshift distribution, while the mock images are simulated in five redshift bins. All these differences combine together and it is not possible to investigate each aspect separately with the current sample. Thus, we cannot pinpoint the property that is the main cause of the poor model performance across domains.

6 SUMMARY AND CONCLUSIVE REMARKS

Tidal interactions are expected to play a critical role in galaxy mass assembly and evolution, but their low surface brightness make these features difficult to detect. Automated methods for the identification and classifications of tidal features will be compulsory for the analysis of large upcoming surveys such as LSST or Euclid.

In this work, we take advantage of the catalogue presented in M22 that provides tidal feature classifications by professional astronomers for a sample of ∼6000 galaxy images from the NewHorizon simulations. This constitutes the largest catalogue of visual identifications of tidal features up to date. The galaxies are simulated at different evolutionary times and redshifts, and HSC-like mock images with different surface brightness limits ($\mu_{lim} = 28$–35 mag arcsec^{-2}) were visually inspected by a varying number of professional astronomers (ranging from 2 to 6).

We use a CNN to train a supervised deep learning binary model which aims to reproduce human visual identification of galaxies with tidal features. For this, we have labelled as positives all the images for which a tidal feature was identified by all the classifiers, regardless of the tidal feature category ($F_{tidal} > 1$, as detailed in Section 3.2) and as negative those with no tidal identification ($F_{tidal} = 0$). We do not use galaxies for which the presence of a tidal feature was uncertain (disagreement between classifiers). In addition to the original sample, we have created shallower images, more similar to current available observations, at $\mu_{lim} = 26, 27$ mag arcsec^{-2}. These images were not classified in M22, and we use their corresponding labels at $\mu_{lim} = 28$ mag arcsec^{-2} as ground truth. We remark the fact that, since the visual classifications are used as input label to the model, any bias present in human classification would be passed on to the deep learning algorithm (see, for example, how the fraction of tidal detections depends on the image properties in Fig. 2). Our main conclusions are:

(i) The deep learning model is successful in reproducing the human identification of images with tidal features in the HSC-mock images, reaching accuracy, precision, and recall values of Acc = 0.84, $P = 0.72$, and $R = 0.85$ for the original test sample, using the optimal threshold, $P_{th} = 0.31$, to select positive cases of tidals.

(ii) The results are surprisingly similar in terms of global accuracy and purity (Acc = 0.85, $P = 0.71$) when the shallower test sample is included, even though these numbers are computed corresponding to the labelling of images one or two orders of magnitude deeper.

(iii) The completeness of the model for the *original + shallow* test sample is smaller than for the *original* one ($R = 0.75$ versus 0.85). There is indeed a clear dependence of the ability of the model to recover tidal features with respect to the image depth: while for $\mu_{lim} > 30$ mag arcsec^{-2} around 90 per cent of the tidal features are recovered, this quantity drops below 50 per cent for $\mu_{lim} < 28$ mag arcsec^{-2} (see Figs 9, 10).

(iv) The accuracy and purity are roughly constant at all surface brightness, hence we conclude that the model is not learning the signal-to-noise of the images, although it is evident that it impacts the classification performance, mostly in terms of completeness, as expected.

(v) The trend with redshift is not so evident, with the larger AUC values obtained at redshift bins $z = 0.05$ and 0.4. The decrease of the fraction of visually identified tidal features at higher redshifts may explain this non-intuitive result (the model is able to correctly recover the true negatives).

(vi) Tidal *streams* and *shells* are the categories easier to identify by the model, with TPR = 1 and 0.87, respectively. On the other hand, *mergers* and *tails* reach only TPR = 0.68, 0.69, respectively.

(vii) When applied to real HSC images with $\mu_{\mathrm{lim}} = 26\,\mathrm{mag\,arcsec^{-2}}$, the performance is significantly worse than on the simulated images (AUC = 0.69), even when transfer learning is applied. This is probably related to the fact that the simulated images are not extremely realistic: they have lower spatial resolution than real images, and do not include background effects. Besides, they span over a wide μ_{lim} range, do not have a uniform redshift coverage, and may not include examples of all observed morphological types and/or features.

The results presented in this work represent an important step in the development of automated tidal feature detection techniques, even if the performance is lower than those found in other astronomical classification tasks like separating elliptical from disc galaxies (reaching accuracy above 97 per cent). Tidal feature detection is a difficult task, given the low surface brightness of the subtle structures that we wish to detect. An additional limitation is the lack of a large, homogeneously observed training sample with certain classifications.

One alternative would be to use 'intrinsic' labels from simulations, derived from dynamics or merger trees. The disadvantage of such labelling is that observational limitations may not always support the classification of an image in accordance with its intrinsic class. In this work, the training data is assembled from human labels. Labelling tidal features via visual inspection is not trivial and the image pre-processing has a significant impact. In addition, classifiers tend to disagree with each other quite often, as shown in M22. Biases in the identification of interacting galaxies by visual classifications have also been reported in Blumenthal et al. (2020). Therefore, it may not even be possible to achieve an accuracy similar to elliptical/spiral separation due to the much greater ambiguity of the classifications.

We are aware of some important efforts of the scientific community towards building large and robust samples of tidal identifications, such as the detailed annotations presented in Sola et al. (2022), Bílek et al. (2020), or the on-going tidal stream survey by Martinez-Delgado et al. (2021), which will certainly help to construct a robust training sample to improve the algorithms for automated detection. Approaches such as domain adaptation (Ćiprijanović et al. 2022), the use of unsupervised learning (e.g. Cheng et al. 2021; Sarmiento et al. 2021), or one-shot learning (Chen et al. 2019) could help to overcome the lack of positive training samples currently available, but we leave these approaches for the forthcoming analysis.

The poorer performance of our tidal identification model in the real HSC-SSP images emphasizes the large dependence of deep learning algorithms on the data they are trained with. As already noted in Bottrell et al. (2019a), Huertas-Company et al. (2019), Ćiprijanović et al. (2022), the importance of using realistic simulations for training the models, including background, real noise, and artifacts, is fundamental to achieving robust results with real data. This should be taken as a warning against applying deep learning models to different data domains without previously assessing their performance on the new domain.

Our results also highlight the need for deep surveys in order to construct complete samples of galaxies showing tidal interactions. Our predictions imply that we need images with $\mu_{\mathrm{lim}} > 30\,\mathrm{mag\,arcsec^{-2}}$ to achieve completeness above 60 per cent, although given the non-representative sample used for the statistical analysis presented in this work our current result is only suggestive of this requirement. For example, as already noted in Bottrell et al. (2019a) and Bickley et al. (2021), for rare objects amongst large data sets (such as the upcoming LSST) the precision, largely dependent on the assumed fraction of positive instances, is paramount. One could increase the completeness by using larger value of P_{th}, even if that would decrease the purity, and complement it with visual inspection of a much smaller sample of galaxies.

The challenges facing the automated detection of tidal features should not prevent us from that endeavour. The scientific return of large samples of galaxies showing tidal features is huge. The detection and characterization of these faint tidal remnants – including measurements of their abundance, width, and shapes/morphology – probe the recent merger activity, disruption mechanisms, and galaxy mass assembly. Furthermore, the characteristics of observed tidal features can constrain the global properties of the stellar and dark matter haloes (Johnston et al. 1999; Sanderson, Helmi & Hogg 2015; Bovy et al. 2016; Pearson et al. 2022), and, consequently, a complementary way to testing cosmological and dark matter theories. These are, indeed, some of the scientific objectives of the recently approved F-ESA mission ARRAKIHS[5] (P.I. R Guzmán), that will image 50 deg^2 of the sky per year down to an unprecedented ultra-low surface brightness in visible infrared bands (31 and 30 mag arcsec^{-2}, respectively). The future of scientific analysis based on tidal features is bright and promising, and this work undoubtedly represents an important step forward towards understanding the requirements of an optimal automated identification of such powerful ingredient for galaxy evolution and cosmological studies.

ACKNOWLEDGEMENTS

---

[5] https://www.cosmos.esa.int/documents/7423467/7423486/ESA-F2-ARRAKIHS-Phase-2-PUBLIC-v0.9.2.pdf

DATA AVAILABILITY

The catalogue used in this article comes from the analysis of M22. The code used for the deep learning algorithm will be shared upon request.

REFERENCES

Aihara H. et al., 2018a, PASJ, 70, S4
Aihara H. et al., 2018b, PASJ, 70, S8
Bickley R. W. et al., 2021, MNRAS, 504, 372
Bílek M. et al., 2020, MNRAS, 498, 2138
Blumenthal K. A. et al., 2020, MNRAS, 492, 2075
Bottrell C., Simard L., Mendel J. T., Ellison S. L., 2019a, MNRAS, 486, 390
Bottrell C. et al., 2019b, MNRAS, 490, 5390
Bovy J., Bahmanyar A., Fritz T. K., Kallivayalil N., 2016, ApJ, 833, 31
Bruzual G., Charlot S., 2003, MNRAS, 344, 1000
Bullock J. S., Johnston K. V., 2005, ApJ, 635, 931
Chen Z., Fu Y., Zhang Y., Jiang Y.-G., Xue X., Sigal L., 2019, IEEE Trans. Image Process., 28, 4594
Cheng T.-Y. et al., 2020, MNRAS, 493, 4209
Cheng T.-Y., Huertas-Company M., Conselice C. J., Aragón-Salamanca A., Robertson B. E., Ramachandra N., 2021, MNRAS, 503, 4446
Ćiprijanović A. et al., 2022, Mach. Learn.: Sci. Techn., 3, 035007
Cole S., Lacey C. G., Baugh C. M., Frenk C. S., 2000, MNRAS, 319, 168
Conselice C. J., Bershady M. A., Jangren A., 2000, ApJ, 529, 886
Conselice C. J., Mundy C. J., Ferreira L., Duncan K., 2022, ApJ, 940, 168
Cooper A. P., D'Souza R., Kauffmann G., Wang J., Boylan-Kolchin M., Guo Q., Frenk C. S., White S. D. M., 2013, MNRAS, 434, 3348
Dieleman S., Willett K. W., Dambre J., 2015, MNRAS, 450, 1441
Domínguez Sánchez H., Huertas-Company M., Bernardi M., Tuccillo D., Fischer J. L., 2018, MNRAS, 476, 3661
Domínguez Sánchez H. et al., 2019, MNRAS, 484, 93
Domínguez Sánchez H., Margalef B., Bernardi M., Huertas-Company M., 2022, MNRAS, 509, 4024
Draine B. T. et al., 2007, ApJ, 663, 866
Dubois Y. et al., 2014, MNRAS, 444, 1453
Dubois Y. et al., 2021, A&A, 651, A109
Duc P.-A. et al., 2015, MNRAS, 446, 120
Fall S. M., Efstathiou G., 1980, MNRAS, 193, 189
Fitts A. et al., 2018, MNRAS, 479, 319
Ghosh A., Urry C. M., Wang Z., Schawinski K., Turp D., Powell M. C., 2020, ApJ, 895, 112
Gwyn S. D. J., 2012, AJ, 143, 38
Hausen R., Robertson B. E., 2020, ApJS, 248, 20
He K., Zhang X., Ren S., Sun J., 2016, in 2016 IEEE Conference on Computer Vision and Pattern Recognition (CVPR). p. 770
Helmi A., White S. D., 1999, MNRAS, 307, 495
Hendel D., Johnston K. V., 2015, MNRAS, 454, 2472
Hernquist L., Quinn P. J., 1989, ApJ, 342, 1
Hood C. E., Kannappan S. J., Stark D. V., Dell'Antonio I. P., Moffett A. J., Eckert K. D., Norris M. A., Hendel D., 2018, ApJ, 857, 144
Huang Q., Fan L., 2022, ApJS, 262, 39
Huertas-Company M., Lanusse F., 2022, Publ. Astron. Soc. Aust., 40, e001
Huertas-Company M. et al., 2015, ApJS, 221, 8
Huertas-Company M. et al., 2019, MNRAS, 489, 1859
Huško F., Lacey C. G., Baugh C. M., 2022, MNRAS, 518, 5323
Iodice E. et al., 2017, ApJ, 839, 21
Ivezić Ž. et al., 2019, ApJ, 873, 111
Javanmardi B. et al., 2016, A&A, 588, A89
Ji I., Peirani S., Yi S. K., 2014, A&A, 566, A97
Johnston K. V., Majewski S. R., Siegel M. H., Reid I. N., Kunkel W. E., 1999, AJ, 118, 1719
Johnston K. V., Bullock J. S., Sharma S., Font A., Robertson B. E., Leitner S. N., 2008, ApJ, 689, 936
Kado-Fong E. et al., 2018, ApJ, 866, 103

Komatsu E. et al., 2011, ApJS, 192, 18
Lacey C., Cole S., 1993, MNRAS, 262, 627
Lanusse F., Ma Q., Li N., Collett T. E., Li C.-L., Ravanbakhsh S., Mandelbaum R., Póczos B., 2018, MNRAS, 473, 3895
Laureijs R. et al., 2011, preprint (arXiv:1110.3193)
Lofthouse E. K., Kaviraj S., Conselice C. J., Mortlock A., Hartley W., 2017, MNRAS, 465, 2895
López-Sanjuan C. et al., 2012, A&A, 548, A7
Lotz J. M., Jonsson P., Cox T. J., Croton D., Primack J. R., Somerville R. S., Stewart K., 2011, ApJ, 742, 103
Lupton R., Blanton M. R., Fekete G., Hogg D. W., O'Mullane W., Szalay A., Wherry N., 2004, PASP, 116, 133
Mancillas B., Duc P.-A., Combes F., Bournaud F., Emsellem E., Martig M., Michel-Dansac L., 2019, A&A, 632, A122
Martin G., Kaviraj S., Devriendt J. E. G., Dubois Y., Laigle C., Pichon C., 2017, MNRAS, 472, L50
Martin G., Kaviraj S., Devriendt J. E. G., Dubois Y., Pichon C., 2018, MNRAS, 480, 2266
Martin G. et al., 2021, MNRAS, 500, 4937
Martin G. et al., 2022, MNRAS, 513, 1459
Martínez-Delgado D., Pohlen M., Gabany R. J., Majewski S. R., Peñarrubia J., Palma C., 2009, ApJ, 692, 955
Martínez-Delgado D. et al., 2010, AJ, 140, 962
Martinez-Delgado D. et al., 2021, AAP, 671, A141
Mihos J. C., Dubinski J., Hernquist L., 1998, ApJ, 494, 183
Mihos J. C., Harding P., Feldmeier J. J., Rudick C., Janowiecki S., Morrison H., Slater C., Watkins A., 2017, ApJ, 834, 16
Miyazaki S. et al., 2012, in McLean I. S., Ramsay S. K., Takami H., eds, SPIE Conf. Ser. Vol. 8446, Ground-based and Airborne Instrumentation for Astronomy IV. SPIE, Bellingham, p. 84460Z
Montes M., Infante-Sainz R., Madrigal-Aguado A., Román J., Monelli M., Borlaff A. S., Trujillo I., 2020, ApJ, 904, 114
Montes M., Brough S., Owers M. S., Santucci G., 2021, ApJ, 910, 45
Morales G., Martínez-Delgado D., Grebel E. K., Cooper A. P., Javanmardi B., Miskolczi A., 2018, A&A, 614, A143
O'Leary J. A., Moster B. P., Naab T., Somerville R. S., 2021, MNRAS, 501, 3215
Pearson S., Price-Whelan A. M., Hogg D. W., Seth A. C., Sand D. J., Hunt J. A. S., Crnojević D., 2022, ApJ, 941, 19
Pillepich A. et al., 2014, MNRAS, 444, 237
Qu Y. et al., 2017, MNRAS, 464, 1659
Robertson B., Bullock J. S., Cox T. J., Di Matteo T., Hernquist L., Springel V., Yoshida N., 2006, ApJ, 645, 986
Rodriguez-Gomez V. et al., 2016, MNRAS, 458, 2371
Rodríguez-Puebla A., Primack J. R., Avila-Reese V., Faber S. M., 2017, MNRAS, 470, 651
Salpeter E. E., 1955, ApJ, 121, 161
Sanderson R. E., Helmi A., Hogg D. W., 2015, ApJ, 801, 98
Sarmiento R., Huertas-Company M., Knapen J. H., Sánchez S. F., Domínguez Sánchez H., Drory N., Falcón-Barroso J., 2021, ApJ, 921, 177
Sola E. et al., 2022, A&A, 662, A124
Spavone M. et al., 2018, ApJ, 864, 149
Spavone M. et al., 2020, A&A, 639, A14
Tan M., Le Q. V., 2019, preprint (arXiv:1905.11946)
Thorp M. D., Bluck A. F. L., Ellison S. L., Maiolino R., Conselice C. J., Hani M. H., Bottrell C., 2021, MNRAS, 507, 886
Valenzuela L. M., Remus R.-S., 2022, preprint (arXiv:2208.08443)
van Dokkum P. G. et al., 2010, ApJ, 709, 1018
Vega-Ferrero J. et al., 2021, MNRAS, 506, 1927
Vera-Casanova A. et al., 2022, MNRAS, 514, 4898
Walmsley M., Ferguson A. M. N., Mann R. G., Lintott C. J., 2019, MNRAS, 483, 2968
Walmsley M. et al., 2022, MNRAS, 509, 3966
Weingartner J. C., Draine B. T., 2001, ApJ, 548, 296
White S. D. M., Frenk C. S., 1991, ApJ, 379, 52
White S. D. M., Rees M. J., 1978, MNRAS, 183, 341

This paper has been typeset from a TEX/LATEX file prepared by the author.